Final-state-resolved mutual neutralization in I$^+$ - I$^-$ collisions

Mathias Poline [1,*], Xiang Yuan [2,3], Sylvain Badin [2,4], MingChao Ji [1], Stefan Rosén,[1] Suvasthika Indrajith [1],
Richard D. Thomas [1], Henning T. Schmidt [1], Henning Zettergren [1], Andre Severo Pereira Gomes [2],
and Nicolas Sisourat[4,*]

[1]*Department of Physics, Stockholm University, Stockholm SE-10691, Sweden*
[2]*Université de Lille, CNRS, UMR 8523, Physique des Lasers, Atomes et Molécules, F-59000 Lille, France*
[3]*Department of Chemistry and Pharmaceutical Science, Faculty of Science, Vrije Universiteit Amsterdam,
de Boelelaan 1083, 1081 HV Amsterdam, Netherlands*
[4]*Sorbonne Université, CNRS, Laboratoire de Chimie Physique Matière et Rayonnement, UMR 7614, F-75005 Paris, France*

We have studied the mutual neutralization reaction of atomic iodine ions (i.e., I$^+$ + I$^-$ → I + I) in a cryogenic double electrostatic ion-beam storage-ring apparatus. Our results show that the reaction forms iodine atoms either in the ground-state configuration (I($5p^5\,^2P^\circ$), ∼40%) or with one atom in an electronically excited state (I($6s\,^2$[2]), ∼60%), with no significant variation over the branching ratios in the studied collision-energy range (0.1–0.8 eV). We estimate the total charge-transfer cross section to be of the order of 10^{-13} cm^2 at 0.1 eV collision energy. *Ab initio* relativistic electronic structure calculations of the potential-energy curves of I$_2$ suggest that the reaction takes place at short internuclear distances. The results are discussed in view of their importance for applications in electric thrusters.

I. INTRODUCTION

Electric thrusters for space vehicles have been used across the world since the 1960s. Since then, they have been deployed on hundreds of satellites and space exploration probes [1,2]. Thanks to the recent increase in available power on spacecraft [1], the full potential of electric propulsion is now achievable. This is demonstrated by the emergence of all-electric communication satellites and projects requiring the deployment of large constellations of small electric-powered satellites [1–3] (see also [4] and references therein).

The basic physical principles of electric thrusters are the following: a plasma is formed by ionizing the propellant, and the ions created are accelerated by electromagnetic fields. The ejection of the accelerated ions produces a thrust to the spacecraft through the conservation of momentum. The efficiency of these systems depends strongly on the total ion density formed in the plasma. An efficient propellant should therefore have high atomic mass and be easy to ionize in order to yield high ion fluxes and exert a large force on the spacecraft. Xenon is currently the propellant of choice (see, e.g., [5] and references therein), owing to its high atomic mass and fairly low ionization potential. However, xenon is rare, is

expensive, and must be stored either in high-pressure tanks or at cryogenic temperatures, significantly impacting the usable volume in satellites.

The iodine molecule is an interesting candidate to replace xenon [6–9] since it also has high atomic mass and low ionization potential. In contrast to xenon, iodine is cheap and exists in the solid state at standard pressure and temperature. These properties result in a storage density of iodine that is 3 times higher than that of xenon under equivalent conditions. In an iodine plasma thruster, the electric energy is used to ionize the iodine molecules to form the plasma. In addition to this ionization, some energy is also inevitably dissipated in other processes, leading to various atomic and molecular iodine species, both neutral and charged. Only ions can be accelerated electrically to participate in the propulsion. However, various reactions taking place in the volume of the plasma can lead to the neutralization of the species, thus causing substantial power loss. Currently, no data are available on these processes, thus impeding the description and modeling of such thrusters.

As a first step to address these issues, we have studied a key reaction in iodine plasmas [10], the mutual-neutralization (MN) reaction of atomic iodine ions:

$$I^+ + I^- \rightarrow I + I + E_K, \qquad (1)$$

where E_K is the kinetic energy released in the process. Recent modeling suggested that this reaction is important to the performance of thrusters [10]. However, the model relies on input from experimental studies that are associated with large uncertainties regarding the actual MN collision partners and the related rates in iodine plasmas [11]. Furthermore, the atoms formed in MN collisions can undergo further reactions [6], whose rates may depend strongly on the final states of the

---

*Corresponding authors: mathias.poline@fysik.su.se;
nicolas.sisourat@sorbonne-universite.fr

reaction products. The present study is therefore needed to improve the modeling of iodine plasma.

In MN reactions, the kinetic energy released E_K is related to the initial- and final-state distributions of the atoms. By measuring E_K, the branching ratios of the different channels in this reaction were determined at collision energies of ~ 0.1 and ~ 0.8 eV. Our results show that (i) the reaction leads to two different sets of product pairs, either a pair of atoms in the ground-state configuration or a pair in which one atom is in its ground state while the other is in the $6s\,^2[2]$ excited state; (ii) these pairs have a population of roughly 40%/60% with no significant dependence on the collision energy in the studied range; and (iii) the total charge-transfer cross section is of the order of 10^{-13} cm^2 at 0.1-eV collision energy. Furthermore, insights into the electron dynamics taking place during the collision are provided by potential-energy curves for I_2, which we have calculated by means of multireference *ab initio* relativistic electronic structure methods. These suggest that the relevant curve crossings leading to the observed final states occur at short internuclear distances.

The outline of this article is as follows: in Sec. II, we briefly describe the theoretical and experimental methods employed to study the mutual neutralization reactions of iodine ions. In Sec. III, the *ab initio* potential-energy curves of I_2 are discussed, and the experimental branching ratios for the different channels in this reaction are reported. The article ends with a summary of this work (Sec. IV).

II. METHODS

A. Theory

The *ab initio* calculations of the electronic states of I_2 were performed with the DIRAC19 release [12] and with a development version (hash 1E798E5) of the DIRAC relativistic electronic structure package [13]. In all calculations we employed the four-component Dirac-Coulomb Hamiltonian, which accounts for scalar and spin-orbit effects at the mean-field level. We employed an uncontracted triple-zeta quality basis set, including three diffuse functions (t-aug-dyall.v3z [14]), in order to accurately compute the Rydberg and ion-pair (IP) states.

The ground and electronically excited states considered here were obtained with the multireference configuration interaction (MRCI) method, as implemented in the KRCI module [15] of DIRAC. In the reference configuration for MRCI we employed 10 electrons distributed over 12 spinors. It includes the valence $\sigma_{1/2}$, $\pi_{1/2}$, $\pi_{3/2}$, $\pi^*_{1/2}$, $\pi^*_{3/2}$, and $\sigma^*_{1/2}$ molecular spinors arising from the p^5 manifold of each atom and ensures a qualitatively correct dissociation behavior for large internuclear distances. We calculated 109 single-point energies within the range of 1.9–10 Å for the potential-energy curves (PECs) and 63 molecular states in total for the $\Omega = 0_g$, 0_u, 1_g, 1_u, 2_g, and 2_u symmetries. Spectroscopic constants for the different (bound) electronic states have been derived from the calculated PECs with the LEVEL [16] program.

Our electronic structure calculations account for spin-orbit coupling from the outset, with systems possessing linear symmetry. Thus, instead of employing the commonly used *LS*-coupling notation to characterize the symmetry of the
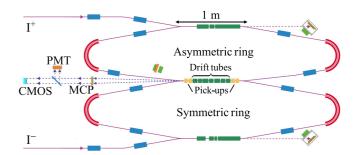

FIG. 1. Schematic of the double electrostatic ion-beam storage ring DESIREE. I^+ and I^- ion beams are created from two different ion sources (see text) and injected into the two rings. In the merged section (drift tubes), the ions interact, and the resulting neutrals are detected by means of a three-dimensional imaging detector consisting of a microchannel plate and phosphor screen based detector (MCP), a CMOS camera, and a PMT.

molecular electronic states, we label them by the value of the projection of the total electronic angular momentum along the internuclear axis Ω. For example, the first $\Omega = 0_g^+$ state corresponds to the $^1\Sigma_g^+$ ground state (for further details on how the DIRAC code handles the attribution of such quantities see Ref. [13]).

B. Experimental details

The experiments were carried out at the double electrostatic ion-beam storage-ring facility Double ElectroStatic Ion Ring ExPEriment (DESIREE) (Stockholm University, Sweden), an ultrahigh-vacuum device operated at cryogenic temperatures of about 13 K. This experimental setup was described previously by Thomas *et al.* [17] (design and technical description), Schmidt *et al.* [18] (first commissioning), and Eklund *et al.* [19] (first mutual neutralization experiment) and is only briefly discussed here.

Positive iodine ions were produced from pure iodine in an electron cyclotron resonance (ECR) ion source, and negative iodine ions were produced from magnesium iodide compounds in a cesium sputtering source. Bending magnets at the exit of the sources were employed to select the ions of interest, after which the two oppositely charged ion beams of ^{127}I were accelerated and injected into the two storage rings.

As shown in Fig. 1, the two rings share a common section in which interactions between the two species may occur. Pickup electrodes, located at the entrance and exit of this merged section, measure the beam positions and were used to optimize the overlap of the two ion beams. The collision energy $E_{c.m.}$ of the reaction was then fine-tuned through the biasing of drift tubes. This applied voltage decelerates (accelerates) the negative (positive) ions to the desired velocities in a small section of this merged region (the biased region), allowing us to constrain the region of low-collision-energy interactions (here chosen to be approximately 16 cm long).

A microchannel-plate (MCP) detector [20] located 1.5 m from this biased region was used to detect the neutralized particles arising from mutual neutralization events and residual gas collisions. Each of these events produced light spots on a phosphor screen located behind the MCP. The resulting

TABLE I. Experimental parameters used during the data acquisitions. They include the energies E_i and currents I_i of the positive (A) and negative (B) ion beams, the potentials applied to the interaction region U, and the center-of-mass collision energy obtained $E_{c.m.}$.

Data set	E_A (keV)	E_B (keV)	I_A (nA)	I_B (nA)	U (V)	$E_{c.m.}$ (eV)
1	13	12	3	8	500	0.07 ± 0.01
2	35	30	15	30	1275	0.10 ± 0.02
3	35	30	15	30	1060	0.80 ± 0.10

photons are guided via optics to a complementary metal oxide semiconductor (CMOS) camera and a multianode photomultiplier tube (PMT), which record the positions and relative arrival times of the particles. The PMT signal-processing system can detect events with an arrival-time difference up to 200 ns. In the unbiased region of the merged section, the relative velocity of the two ions is such that the arrival-time differences are well outside this time window. Thus, these events do not interfere with the data from reactions occurring in the biased region.

C. Branching-ratio calculations

For an MN event occurring at a distance L from the detector, the separation between two neutral particles formed in the reaction, as recorded by the detection system, is given by

$$r = \sqrt{r_\parallel^2 + r_\perp^2} \approx \sqrt{\frac{2(E_K + E_{c.m.})}{\mu}}\frac{L}{v}, \qquad (2)$$

where $r_\parallel$ is the projected transverse distance, recorded by the camera, $r_\perp \approx v\Delta t$ is an approximation of the third dimensional component (v is the average velocity of the reactants), and μ is the reduced mass of the ions. Here, $E_{c.m.}$ is the center-of-mass kinetic energy before the interaction, and E_K is the kinetic energy released in the specific reaction channel.

This particular three-dimensional imaging technique of two particles was first introduced by Amitay and Zajfman [21] for the study of the dissociative recombination reaction [22–24] but has since been employed for a number of MN systems, such as Li$^+$/D$^-$ [19,25], Mg$^+$/D$^-$ [26], and O$^+$/O$^-$ [27,28]. The resulting spectrum represents a distribution of the final-state center-of-mass kinetic energy over the longitudinal extension of the interaction region and the collision-energy spread. By simulating these distributions using the Monte Carlo method and fitting them to the data, the branching ratios can be extracted [19,29]. They are corrected for the energy-dependent efficiency related to the angular acceptance of the detectors (for more details see Ref. [28]).

Table I shows the experimental parameters used during the three experimental runs: In the first run, data were acquired using slower ion beams in order to investigate the low kinetic-energy release E_K channels in detail; in the other two runs, data were acquired with the aim of measuring the final-state distributions of all energetically open channels at two different collision energies.

In order to maximize the range of product kinetic energies that could be detected and obtain satisfying rates, higher beam energies and currents were used in the two later data sets, resulting in larger background contributions. These mainly arise from collisions between stored ions and residual-gas
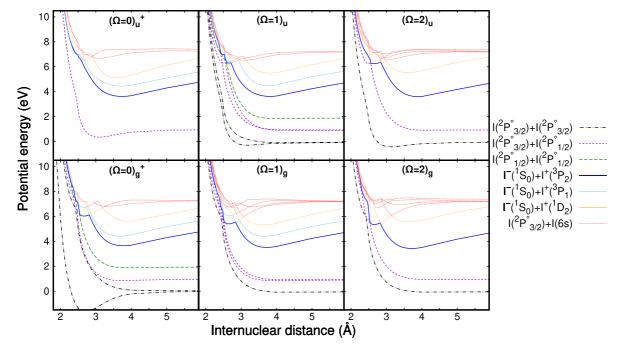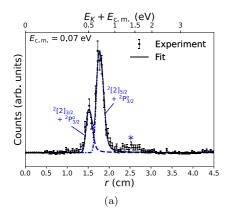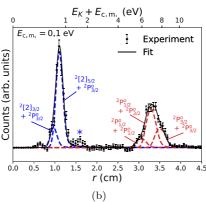

FIG. 2. MRCI PECs of 51 electronic states (including Rydberg and IP) of I$_2$, classified in terms of the projection of the total electronic angular momentum Ω. Twelve $(\Omega = 0)^-_g$ and $(\Omega = 0)^-_u$ states are not shown here since there is no I$^+$($^3P_2$) + I$^-$($^1S_0$) state with this symmetry. The energies (in eV) have been scaled so that the zero corresponds to twice the energy of the $^2P_{3/2}$ ground state of the isolated iodine atom. See Table III for the energies of the different asymptotes. Detailed views of the PECs at short internuclear distances are shown in Fig. 5 in the Appendix.
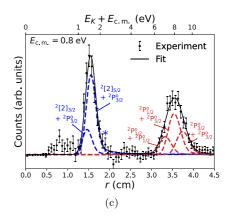
FIG. 3. Yields of neutral pairs as a function of the separation r between the products at center-of-mass collision energies of (a) 0.07 eV, (b) 0.1 eV, and (c) 0.8 eV. The top scale shows the corresponding center-of-mass kinetic energy after the reaction [Eq. (2)]. The solid curve results from a fit of the simulated distributions of ground-state–excited-state pairs [blue line; Eq. (3)] and ground-state-configuration pairs [red line; Eq. (4)]. The asterisks indicate contributions from metastable cations (not included in the fit). The background has been subtracted (see Fig. 6 in the Appendix for original spectra).

molecules as well as false coincidences. The majority of the background could be filtered out by excluding events for which the center-of-mass position of the two products on the imaging detector was outside a 5-mm range. However, a non-negligible number of events remained after this selection, in particular for measurements with low signal to background ratio. The filtered-out events were then used as a model for this remaining background and were subsequently subtracted from the spectra. For more details see the Appendix.

D. Reaction cross-section estimate

In order to extract MN reaction cross sections, it is necessary to determine the spatial distributions of the interacting particle beams. Currently, a method to derive this overlap (form factor) with high precision is not available at DESIREE. Additionally, it may vary between different experiments since the storing of merged beams requires adjusting the ion optics based on the mass ratio and energies of the two ions. The cross section may therefore be only roughly estimated based on the observed rates relative to other previously studied systems with known cross sections and is subject to large uncertainties. However, given the absence of any experimental or theoretical estimate for this particular collision system, we have made such an evaluation, which is presented in the results section.

III. RESULTS AND DISCUSSION

A. Theoretical results

In order to get insights into the MN dynamics, we report the potential-energy curves of I_2 in Fig. 2 (a detailed discussion of these curves is given in the Appendix). At the collision energies investigated in this work, electronic processes take place mainly around the avoided crossings. Assuming the system starts in the lowest ion-pair state [i.e., $I^+(^3P_2) + I^-(^1S_0)$; blue curve in Fig. 2], one can, in principle, study the paths to a given final state for each symmetry. Since the asymptotic energy of the ion-pair state lies above the neutral excited-state–ground-state pair, the reaction may result in

the formation of an electronically excited iodine atom, i.e.,

$$I^+ + I^- \rightarrow \begin{cases} I(6s\ ^2[2]_{3/2}) + I(5p^5\ ^2P^\circ_{3/2}) + 0.44\text{ eV}, \\ I(6s\ ^2[2]_{5/2}) + I(5p^5\ ^2P^\circ_{3/2}) + 0.62\text{ eV}. \end{cases} \quad (3)$$

As there are too many avoided crossings between the states, an appropriate simulation of the collision dynamics is necessary to study the pathway to these channels. However, the path to the lowest states of I_2 is fairly simple: For all symmetries the lowest ion-pair state exhibits first an avoided crossing with the curves corresponding to $I(^2P^\circ_{3/2}) + I(6s)$ (here shown in red) at an internuclear distance between 2.5 and 3 Å. At shorter internuclear distances, these curves can cross the ground-state-configuration curves, resulting in the following channels:

$$I^+ + I^- \rightarrow \begin{cases} I(5p^5\ ^2P^\circ_{1/2}) + I(5p^5\ ^2P^\circ_{1/2}) + 5.51\text{ eV}, \\ I(5p^5\ ^2P^\circ_{1/2}) + I(5p^5\ ^2P^\circ_{3/2}) + 6.45\text{ eV}, \\ I(5p^5\ ^2P^\circ_{3/2}) + I(5p^5\ ^2P^\circ_{3/2}) + 7.39\text{ eV}. \end{cases} \quad (4)$$

Therefore, the simplest path to the lowest states of I_2 is through a highly excited state followed by a deexcitation of the excited iodine atom at closer distances between the collision partners.

We note that avoided crossings between the lowest ion-pair state and these excited-state–ground-state pair states also occur at larger internuclear distances (~23 Å). However, using a Landau-Zener approach and the Olson semiempirical model (see [30], Eq. (13)), we estimate that the electronic couplings at these avoided crossings are negligible. The dynamics of the reaction are therefore expected to take place at the avoided crossings presented in Fig. 2, for which more advanced modeling is necessary, as the current approach is not applicable to nonisolated crossings occurring at short internuclear distances.

B. Experimental results

The yields of neutral pairs as a function of the separation r between the products for the three acquired data sets (see Table I) are shown in Figs. 3(a), 3(b), and 3(c). As different
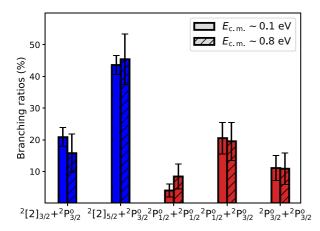
FIG. 4. Branching ratios of the mutual neutralization of I^+ with I^- at the two measured collision energies.

TABLE II. Experimental branching ratios of the different channels at collision energies of 0.1 and 0.8 eV.

Product channel	E_K (eV)	Expt., 0.1 eV	Expt., 0.8 eV
$^2[2]_{3/2} + {}^2P^o_{3/2}$	0.44	21% $\pm$ 3%	16% $\pm$ 6%
$^2[2]_{5/2} + {}^2P^o_{3/2}$	0.62	44% $\pm$ 3%	45% $\pm$ 8%
$^2P^o_{1/2} + {}^2P^o_{1/2}$	5.51	4% $\pm$ 2%	8% $\pm$ 4%
$^2P^o_{1/2} + {}^2P^o_{3/2}$	6.45	20% $\pm$ 5%	20% $\pm$ 6%
$^2P^o_{3/2} + {}^2P^o_{3/2}$	7.39	11% $\pm$ 4%	11% $\pm$ 5%
$^2[2] + {}^2P^o$	$\sim$0.5 eV	65% $\pm$ 1%	61% $\pm$ 3%
$^2P^o + {}^2P^o$	$\sim$6.5 eV	35% $\pm$ 1%	39% $\pm$ 3%

beam energies and collision energies were used for the different data sets, the measured separations then correspond to different final kinetic energies [see Eq. (2)], as highlighted in the top scales of Fig. 3, and hence different final states [Eqs. (3) and (4)]

For the first spectrum [Fig. 3(a)], at (0.07 ± 0.01)-eV collision energy, slower ion beams were used in order to resolve the channels resulting in iodine in the $6s\,{}^2[2]$ excited state. Thus, the separations correspond to kinetic energies only up to 3 eV. The two channels [Eq. (3)], corresponding to the spin-orbit splitting of this excited state, can be clearly distinguished in the spectrum, with the $J = 5/2$ state found to dominate. In the second data set [Fig. 3(b)], a similar collision energy was achieved, namely, 0.10 ± 0.02 eV. The same two peaks [from Fig. 3(a)] are then located at lower separations (around 1 cm) due to the higher beam energies used but are no longer resolved. However, an additional peak appears at larger separations, corresponding to pairs of iodine atoms in the ground-state configuration [Eq. (4)]. Since the broadening of the distributions scales with kinetic energy, the individual J-state pairs are not resolved, but the width of the peak indicates that contributions from all three channels are present.

The observed rate for this measurement was found to be commensurate with the O^+/O^- collision system previously studied at DESIREE [28], for which the cross section is well known [27]. We therefore estimate the cross section to be in the range of 10^{-13} cm^2 (± 1 order of magnitude) at this collision energy ($\sim$0.1 eV).

In the third measurement [Fig. 3(c)], the same beam energies as in Fig. 3(b) were used, but the drift tubes were biased to yield a slightly higher collision energy, i.e., 0.80 ± 0.10 eV. This results in a lower count rate due to the expected $1/E_{c.m.}$ cross section dependence on the collision energy, as well as additional broadening and a shift in the separations. However, the two main peaks are still fully resolved and within the detectable range.

For the three spectra, the results from the fits of the simulated distributions are shown as solid black lines, with the individual distributions shown by colored lines: blue for the excited-state–ground-state pairs and red for the different ground-state-configuration pairs. While the peaks are found to become broader as the collision energy increases, the relative

intensities appear to be mostly unchanged. In addition, two small features appear to not correspond to any of the channels: One at short separations, below the lower energetic channels, is believed to be an artifact of the background model used. The second one, around 1.5 eV, is likely to be a contribution from the first fine-structure state of the cation, namely, $I^+({}^3P_0)$. Since the state is about 0.8 eV above the ground state, it can be expected to be populated to some degree when produced in an ECR source. The observed peak positions (marked with an asterisk in the spectra) are found to correspond to the channels of Eq. (3) with this additional energy. In the higher-collision-energy measurement [Fig. 3(c)], the peak is not observed as it cannot be resolved from the main peak. Storage of up to 20 s did not reveal any change in the signal, suggesting that the metastable level lives for a longer time. This can be explained by the necessity of a quadrupole transition ($\Delta J = 2$) for decay to the ground state.

Based on the fits, the branching ratios were extracted, with the lower-collision-energy measurement ($E_{c.m.} \sim 0.07$ eV) used to determine the relative intensity of the two excited channels at 0.1-eV collision energy. This is motivated as the branching ratios are not expected to change drastically over such a small range of collision energies. The results are presented in Fig. 4, with the full details presented in Table II.

All energetically open channels are found to be populated to some extent, with the $^2[2]_{5/2} + {}^2P^o_{3/2}$ channel found to dominate at the measured collision energies. For the ground-state-configuration pairs, $^2P^o_{1/2} + {}^2P^o_{3/2}$ is favored, while a lower population is observed for the $J = 1/2$ pair compared to the $J = 3/2$ pair. As the individual channels are not fully resolved, the branching ratios have rather large uncertainties, as indicated by the error bars. The two main peaks are, however, clearly separated, and thus, their total branching ratios can be determined directly by evaluating the area under the respective peaks. The uncertainties are then given by the counting statistics and the error in the background. These smaller errors are shown in the last two rows of Table II. The results show that the branching ratios do not differ significantly for the two energies considered.

IV. SUMMARY

In this work, we have studied the mutual neutralization of I^+ with I^-, using *ab initio* relativistic electronic structure calculations and merged beam techniques at the double electrostatic ion-beam storage ring DESIREE. We have measured

TABLE III. Dissociation relationships of I_2. The molecular state is identified by the projection of total electronic angular momentum Ω. The number of states for each symmetry of the Ω state is given in parentheses.

		Energy level (eV)	
Dissociation limits	Molecular states	MRCI (this work)	Expt. [35]
$^2P^\circ_{3/2} + {}^2P^\circ_{3/2}$	$2_g(1), 1_g(1), 0_g(2), 2_u(1), 1_u(2), 0_u(2)$	0	0
$^2P^\circ_{1/2} + {}^2P^\circ_{3/2}$	$2_g(1), 1_g(2), 0_g(2), 2_u(1), 1_u(2), 0_u(2)$	1.04	0.943
$^2P^\circ_{1/2} + {}^2P^\circ_{1/2}$	$0_g(1), 1_u(1), 0_u(1)$	1.99	1.885
$^2[2]_{5/2} + {}^2P^\circ_{3/2}$	$2_g(3), 1_g(4), 0_g(4), 2_u(3), 1_u(4), 0_u(4)$	6.629	6.774
$^2[2]_{3/2} + {}^2P^\circ_{3/2}$	$2_g(2), 1_g(3), 0_g(4), 2_u(2), 1_u(3), 0_u(4)$	7.248	6.954

the branching ratios of the different channels using product-imaging methods combining position and timing information. Our results show that the reaction forms either high-kinetic-energy iodine neutral pairs in the ground-state configuration or slow neutral pairs with one iodine atom in the $6s\,^2[2]$ excited state, through avoided crossings at short internuclear distances. Experimentally, these two channels were found to have a population of about 40%/60%, with no significant dependence on the collision energy in the studied range (0.1–0.8 eV) and with an observed rate commensurate with a previously studied system [28] (cross section of $\sim 10^{-13}$ cm^2 at 0.1-eV collision energy). These results are relevant to the modeling and diagnostics of low-temperature iodine plasmas [31], which are promising candidates as propellants for electric space propulsion. Data on recombination processes are essential to model these plasmas, as these reactions can have substantial effects on the efficiency and ignition time of engines [32]. Furthermore, the atoms formed after MN can undergo further reactions. For example, in [6,10] the authors consider atomic iodine excitation and ionization by electron impact as well as surface recombination. However, they used data that were obtained for iodine in the ground electronic state. The cross sections of these reactions are expected to be different for electronic excited states of iodine. Knowledge of the final-state distribution of the MN reaction, as provided in the present study, is therefore essential to obtain a more accurate description of iodine plasmas. The results discussed here will be combined with theoretical calculations in order to develop and improve the accuracy in modeling mutual neutralization reactions involving iodine species, efforts which will be extended to include more complex reactions involving molecular ions.

TABLE IV. Spectroscopic constants of the lowest four bound Ω states of I_2.

State	T_e (cm^{-1})	R_e (Å)	ω_e (cm^{-1})	Method
$X\,0^+_g$	0	2.717	236.4	MRCI (this work)
	0	2.651	215.9	CASPT2 [34]
	0	2.666	214.5	Exp. [36]
$A\,2_u$	10119	3.124	117.7	MRCI (this work)
		3.014	124.0	CASPT2 [34]
	10042	3.073	108.3	Exp. [36]
$A\,1_u$	11162	3.173	92.0	MRCI (this work)
		3.040	114.6	CASPT2 [34]
	10907	3.114	93.0	Exp. [36]
$B\,0^+_u$	15915	3.089	112.6	MRCI (this work)
		2.991	135.3	CASPT2 [34]
	15769	3.025	125.7	Exp. [36]

TABLE V. Spectroscopic constants of the ion-pair states of I_2. Experimental values (taken from [36] and references therein) are given in parentheses.

State	T_e (cm^{-1})	R_e (Å)	Dissociation limits
$D'\,2_g$	40764 (40388)	3.712 (3.594)	$^3P_2 + {}^1S_0$
$\beta\,1_g$	41438 (40821)	3.721 (3.607)	$^3P_2 + {}^1S_0$
$D\,0^+_u$	42314 (41026)	3.737 (3.584)	$^3P_2 + {}^1S_0$
$E\,0^+_g$	42499 (41411)	3.773 (3.647)	$^3P_2 + {}^1S_0$
$\gamma\,1_u$	42315 (41621)	3.814 (3.683)	$^3P_2 + {}^1S_0$
$\delta\,2_u$	42162 (41787)	3.900 (3.787)	$^3P_2 + {}^1S_0$
$f\,0^+_g$	47971 (47026)	3.692 (3.574)	$^3P_0 + {}^1S_0$
$g\,0^-_g$	48717 (47086)	3.672 (3.572)	$^3P_1 + {}^1S_0$
$F\,0^+_u$	48961 (47217)	3.712 (3.600)	$^3P_0 + {}^1S_0$
$G\,1_g$	48694 (47559)	3.654 (3.549)	$^3P_1 + {}^1S_0$
$H\,1_u$	49327 (48280)	3.749 (3.653)	$^3P_1 + {}^1S_0$
$h\,0^-_u$	49467 (48646)	3.899 (3.780)	$^3P_1 + {}^1S_0$
$F'\,0^+_u$	54363 (51706)	3.557 (3.479)	$^1D_2 + {}^1S_0$
1_g	55934 (53216)	3.623 (3.522)	$^1D_2 + {}^1S_0$
$f'\,0^+_g$	58306 (55409)	3.963 (3.825)	$^1D_2 + {}^1S_0$

APPENDIX

Table III lists the five lowest dissociation limits of I_2. When considering spin-orbital coupling, there are three valence channels for $I(5p^5) + I(5p^5)$, $^2P^\circ_{3/2} + {}^2P^\circ_{3/2}$, $^2P^\circ_{1/2} + {}^2P^\circ_{3/2}$, and $^2P^\circ_{1/2} + {}^2P^\circ_{1/2}$, as well as two Rydberg channels for $I(5p^46s^1) + I(5p^5)$, $^2[2]_{5/2} + {}^2P^\circ_{3/2}$ and $^2[2]_{3/2} + {}^2P^\circ_{3/2}$. The corresponding energy gaps of $^2P^\circ_{3/2} - {}^2P^\circ_{1/2}$ and $^2[2]_{5/2} - {}^2P^\circ_{3/2}$ are 1.0 and 6.63 eV, which are in reasonable agreement with experimental values of 0.94 and 6.77 eV, respectively. On the other hand, for the separation of the $6s$ Rydberg state $^2[2]_{3/2} - {}^2[2]_{5/2}$, the computed value of 0.62 eV is higher than the available experimental value of 0.18 eV.

1. Valence states

There are a total of 22 valence states corresponding to the lowest three dissociation limits, and as can be seen from Fig. 2 (see Fig. 5 for detailed views of the MRCI PECs), most of the molecular states are either repulsive states or quasibound states except for four states: $X\ 0_g^+$, $A\ 2_u$, $A\ 1_u$, and $B\ 0_u^+$, which are consistent with experimental results. The spectroscopic constants of these four states, including equilibrium distance R_e, adiabatic excitation energy T_e, and vibrational constant ω_e, are compared to experimental data

and recent complete active space with second-order perturbation theory correction (CASPT2) results in Table IV. It can be seen from Table IV that our calculations predict T_e rather well, showing average errors no larger than 200 cm^{-1}. For the equilibrium distance, the difference between MRCI and the experimental value is nearly identical to those of CASPT2.

Apart from these valence excited states, we also observe several Rydberg states at energies around 56 000, 61 000, and 67 000 cm^{-1}. We note R_e of such Rydberg states are around 2.66 Å, which is close to R_e of ground-state $X^2\Pi_{3/2g}$ of I_2^+ [33]. So they may belong to a Rydberg series, which converges on the ionization energy threshold associated with the ground state of I_2^+.

2. Ion-pair states

The ion-pair states exhibit dominantly a repulsive Coulomb character. We also fit the corresponding spectroscopic constants of the bound states by LEVEL according to the PECs. The result for T_e and R_e are collected in Table V for comparison.

The total of 18 IP states correspond to four different atomic states of I^+: $^3P_2$, $^3P_1$, $^3P_0$, and $^1D_2$. There is a systematic difference for R_e. The computed R_e values are larger than the experimental ones by about 0.1 Å. For the adiabatic excitation energy, the deviations show a pattern indicated in the CASPT2 calculation [34]; that is, the difference in R_e between gerade states is smaller than that of the ungerade states.

3. Background subtraction

The experimental distributions prior to background subtraction are shown in Fig. 6. This signal corresponds to
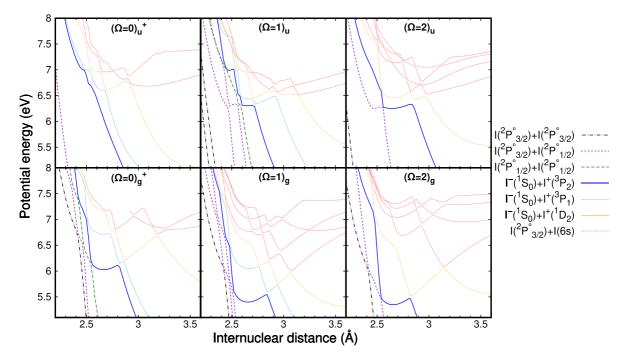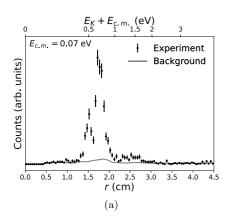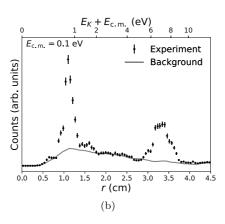

FIG. 5. Detailed views of the MRCI PECs of the electronic states of I_2 at short internuclear distances. Note that the energy for the highest state of symmetry 0_g^+ could not be computed below 2.9 A within the implementation of our method, as seen in the bottom left panel.
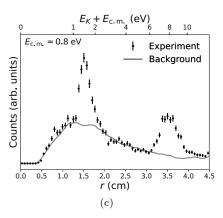
FIG. 6. Spectra from Fig. 3 prior to background subtraction. The background model, which is based on the excluded events in the data analysis, as described in Sec. A3, was fitted to the data and is shown here as a solid gray line.

the data for which the center-of-mass of the two particles is within a 5-mm radius and contains both MN events and background. Outside this radius, the signal should contain only background. Assuming the center-of-mass distribution of the background is random, this signal may be used as a model for the background. An initial fit was first made with

this model based on the data ranges in which no signal is expected to be present [i.e., where r deviates from the simulated distributions of Eqs. (3) and (4)] and is shown as a gray line in Fig. 6. This background model was then subtracted to yield the background-corrected spectra presented in Fig. 3.

[1] S. Mazouffre, Plasma Sources Sci. Technol. **25**, 033002 (2016).

[2] I. Levchenko, S. Xu, G. Teel, D. Mariotti, M. L. R. Walker, and M. Keidar, Nat. Commun. **9**, 879 (2018).

[3] E. Y. Choueiri, J. Propul. Power **20**, 193 (2004).

[4] R. Lucken, Ph.D. thesis, Université Paris Saclay, 2019.

[5] V. Croes, A. Tavant, R. Lucken, R. Martorelli, T. Lafleur, A. Bourdon, and P. Chabert, Phys. Plasmas **25**, 063522 (2018).

[6] P. Grondein, T. Lafleur, P. Chabert, and A. Aanesland, Phys. Plasmas **23**, 033514 (2016).

[7] K. Holste, W. Gärtner, D. Zschätzsch, S. Scharmann, P. Köhler, P. Dietz, and P. J. Klar, Eur. Phys. J. D **72**, 9 (2018).

[8] B. D. Prince, D. J. Levandier, and R. J. Bemish, in *Proceedings of the 53rd AIAA/SAE/ASEE Joint Propulsion Conference* (AIAA Press, Atlanta GA, 2017).

[9] P. Dietz, W. Gärtner, Q. Koch, P. E. Köhler, Y. Teng, P. R. Schreiner, K. Holste, and P. J. Klar, Plasma Sources Sci. Technol. **28**, 084001 (2019).

[10] D. Levko and L. L. Raja, J. Appl. Phys. **130**, 173302 (2021).

[11] T. H. Y. Yeung, Proc. Phys. Soc. **71**, 341 (1958).

[12] A. S. P. Gomes, T. Saue, L. Visscher, H. J. A. Jensen, R. Bast, I. A. Aucar, V. Bakken, K. G. Dyall, S. Dubillard, U. Ekström, E. Eliav, T. Enevoldsen, E. Faßhauer, T. Fleig, O. Fossgaard, L. Halbert, E. D. Hedegård, T. Helgaker, B. Helmich-Paris, and S. Yamamoto, DIRAC19, version 19.0, Zenodo, https://doi.org/10.5281/zenodo.3572669.

[13] T. Saue *et al.*, J. Chem. Phys. **152**, 204104 (2020).

[14] K. G. Dyall, Theor. Chem. Acc. **115**, 441 (2006).

[15] T. Fleig, J. Olsen, and L. Visscher, J. Chem. Phys. **119**, 2963 (2003).

[16] R. J. Le Roy, J. Quantun Spectrosc. Radiat. Transfer **186**, 167 (2017).

[17] R. D. Thomas *et al.*, Rev. Sci. Instrum. **82**, 065112 (2011).

[18] H. T. Schmidt *et al.*, Rev. Sci. Instrum. **84**, 055115 (2013).

[19] G. Eklund, J. Grumer, S. Rosén, M. C. Ji, N. Punnakayathil, A. Källberg, A. Simonsson, R. D. Thomas, M. H. Stockett, P. Reinhed, P. Löfgren, M. Björkhage, M. Blom, P. S. Barklem, H. Cederquist, H. Zettergren, and H. T. Schmidt, Phys. Rev. A **102**, 012823 (2020).

[20] S. Rosén, H. T. Schmidt, P. Reinhed, D. Fischer, R. D. Thomas, H. Cederquist, L. Liljeby, L. Bagge, S. Leontein, and M. Blom, Rev. Sci. Instrum. **78**, 113301 (2007).

[21] Z. Amitay and D. Zajfman, Rev. Sci. Instrum. **68**, 1387 (1997).

[22] D. Zajfman, Z. Amitay, M. Lange, U. Hechtfischer, L. Knoll, D. Schwalm, R. Wester, A. Wolf, and X. Urbain, Phys. Rev. Lett. **79**, 1829 (1997).

[23] Z. Amitay, A. Baer, M. Dahan, J. Levin, Z. Vager, D. Zajfman, L. Knoll, M. Lange, D. Schwalm, R. Wester, A. Wolf, I. F. Schneider, and A. Suzor-Weiner, Phys. Rev. A **60**, 3769 (1999).

[24] R. D. Thomas, Mass Spectrom. Rev. **27**, 485 (2008).

[25] T. Launoy, J. Loreau, A. Dochain, J. Liévin, N. Vaeck, and X. Urbain, Astrophys. J. **883**, 85 (2019).

[26] J. Grumer, G. Eklund, A. M. Amarsi, P. S. Barklem, S. Rosén, M. C. Ji, A. Simonsson, H. Cederquist, H. Zettergren, and H. T. Schmidt, Phys. Rev. Lett. **128**, 033401 (2022).

[27] N. de Ruette, A. Dochain, T. Launoy, R. F. Nascimento, M. Kaminska, M. H. Stockett, N. Vaeck, H. T. Schmidt, H. Cederquist, and X. Urbain, Phys. Rev. Lett. **121**, 083401 (2018).

[28] M. Poline, A. Dochain, S. Rosén, J. Grumer, M. Ji, G. Eklund, A. Simonsson, P. Reinhed, M. Blom, N. S. Shuman, S. G. Ard, A. A. Viggiano, M. Larsson, H. Cederquist, H. T. Schmidt, H. Zettergren, X. Urbain, P. S. Barklem, and R. D. Thomas, Phys. Chem. Chem. Phys. **23**, 24607 (2021).

[29] G. Eklund, J. Grumer, P. S. Barklem, S. Rosén, M. C. Ji, A. Simonsson, R. D. Thomas, H. Cederquist, H. Zettergren, and H. T. Schmidt, Phys. Rev. A **103**, 032814 (2021).

[30] R. E. Olson, J. R. Peterson, and J. Moseley, J. Chem. Phys. **53**, 3391 (1970).

[31] L. L. Alves, A. Bogaerts, V. Guerra, and M. M. Turner, Plasma Sources Sci. Technol. **27**, 023002 (2018).

[32] S. Williams, A. Midey, S. Arnold, P. Bench, A. A. Viggiano, R. Morris, L. Maurice, and C. Carter, in *Proceedings of the 9th International Space Planes and Hypersonic Systems and Technologies Conference* (AIAA Press, Norfolk, VA, 2012).

[33] L.-H. Deng, Y.-Y. Zhu, C.-L. Li, and Y.-Q. Chen, J. Chem. Phys. **137**, 054308 (2012).

[34] V. A. Alekseev, Opt. Spectrosc. **116**, 329 (2014).

[35] A. Kramida, Yu. Ralchenko, J. Reader, and NIST ASD Team, NIST Atomic Spectra Database (version 5.9), National Institute of Standards and Technology, https://doi.org/10.18434/T4W30F.

[36] S. Lukashov, A. Petrov, and A. Pravilov, *The Iodine Molecule* (Springer, Cham, 2018).